Carbon 186 (2022) 227–237

Contents lists available at ScienceDirect

Carbon

journal homepage: www.elsevier.com/locate/carbon

Research Paper

Ultrafast synchrotron X-ray imaging and multiphysics modelling of liquid phase fatigue exfoliation of graphite under ultrasound

Ling Qin [a], Barbara M. Maciejewska [b], Tungky Subroto [c], Justin A. Morton [d], Kyriakos Porfyrakis [e], Iakovos Tzanakis [b, d], Dmitry G. Eskin [c], Nicole Grobert [b, g], Kamel Fezzaa [f], Jiawei Mi [a, *]

[a] Department of Engineering, University of Hull, Hull, HU6 7RX, UK
[b] Department of Materials, University of Oxford, Oxford, OX1 3PH, UK
[c] Brunel Centre for Advanced Solidification Technology, Brunel University London, Uxbridge, UB8 3PH, UK
[d] Department of Mechanical Engineering and Mathematical Sciences, Oxford Brookes University, Oxford, OX3 0BP, UK
[e] Faculty of Engineering and Science, University of Greenwich, Kent, ME4 4TB, UK
[f] The Advanced Photon Source, Argonne National Laboratory, Argonne, 60439, USA
[g] Williams Advanced Engineering, Grove, OX12 0DQ, UK

ARTICLE INFO

Article history:
Received 19 August 2021
Received in revised form
1 October 2021
Accepted 4 October 2021
Available online 7 October 2021

Keywords:
Ultrafast synchrotron X-ray phase-contrast imaging
2D layered graphite materials
Multi-physics modelling
Liquid-phase exfoliation
Ultrasound
Exfoliation dynamics

ABSTRACT

Ultrasound-assisted liquid phase exfoliation is a promising method for manufacturing of 2D materials in large scale and sustainable manner. A large number of studies using *ex-situ* nano/micro structural characterization techniques have been made to investigate the underlying mechanisms, aiming to understand the exfoliation dynamics. Due to the complex multiphysics and multi-length nature of the process, those *ex-situ* methods cannot provide the real-time and *in-situ* dynamic information for understanding how exactly layer exfoliation starts and grows under ultrasound. Here, we used the ultrafast synchrotron-X-ray phase-contrast imaging (a combined temporal resolution of 3.68 μs and a spatial resolution of 1.9 μm/pixel) to study the exfoliation dynamics in real time and operando condition. We revealed, for the first time, the fatigue exfoliation phenomenon at the graphite surface caused by the imploding ultrasonic bubbles occurring cyclically in line with the ultrasound frequency. A multiphysics numerical model was also developed to calculate the shock wave produced at bubble implosion and the resulting cyclic and impulsive tensile and shear stresses acting on the graphite surface. Our research reveals that the graphite layer exfoliation rate and efficiency are predominantly determined by the number of imploding bubbles inside the effective cavitation bubble zone. The findings are valuable for developing industrial upscaling strategies for ultrasound processing of 2D materials.

1. Introduction

Two-dimensional (2D) materials with exceptional chemical, physical and mechanical properties are the essential and fundamental building blocks for the next-generation multifunctional devices and components, for example, in electronic and optoelectronic devices, sensors, energy storage, catalysis, membranes, etc [1–3]. The current challenge of manufacturing 2D materials is to develop efficient, cost-effective and sustainable technologies for making large 2D sheets in large quantity [4,5]. Ultrasound-assisted liquid-phase exfoliation (ULPE) has been identified as one of the promising technical routes for producing 2D large-size monolayer or multilayer sheets (typically ~1 μm long and ~1–10 atomic layers thick) with far fewer defects and less oxidation [5–8]. In the past 10 years or so, extensive research concerning the fundamentals and efficiency of ultrasound processing of different types of bulk 2D materials has been carried out [9–14]. For example, Alaferdov, et al. [15] used a low power ultrasound bath (100 W, 37 kHz) to make graphite nanoflakes from natural graphite powders of 1–3 mm. They suggested that the shock waves and microjet flow produced by the cavitation bubbles collapsed near the graphite flake surface were big enough to break the graphite polycrystals. The pressure required to separate two graphene sheets is estimated to be 7.2 MPa. Other mechanisms [8] proposed include i) unbalanced

* Corresponding author.
E-mail address: J.Mi@hull.ac.uk (J. Mi).

https://doi.org/10.1016/j.carbon.2021.10.014

compressive forces acting on two adjacent layers cause a shear-induced exfoliation or ii) microjets acting as wedges in the graphite interlayers and induce exfoliation. Recently, Li et al. [16] studied, in an *ex-situ* manner, the time-evolved process of ultrasound exfoliation of graphite flakes. They can only characterize the after ultrasound processed flake surfaces in different time intervals using electron microscopy. They proposed that graphite flakes to graphene under ultrasound take place in three distinct stages. However, until now, systematic real-time and *in-situ* studies of the ultrasound layer exfoliation dynamics have not been seen reported. It is mainly due to the experimental challenge and difficulty in capturing the highly transient and dynamic phenomena in the liquid exfoliation process under ultrasound, e.g. the dynamic changes of the alternating acoustic pressure and/or collapsing bubbles occurring at μs and ns time scale. In this aspect, cavitation phenomenon and exfoliation dynamics have been mainly studied using numerical simulation [17,18] or molecular dynamics simulations [19,20]. Modelling and simulation can provide more quantitative information about the acoustic pressure transmission and distribution in the liquid media; as well as calculate the shock wave released kinetic energy and the stresses acting on the bulk materials when cavitation bubble imploded on top of the bulk materials surface. However, because of the lack of real-time collected experimental data, there are problems in the validation of those models, especially for the initial or boundary conditions. Most models used empirically or oversimplified assumptions in their models and simulations, affecting greatly the robustness and accuracy of the simulated results. Hence, there are still some key scientific issues remained unsolved concerning the time-evolved exfoliation dynamics. Firstly, it is not clear how exactly the 2D layer exfoliation starts in a liquid medium at the early stage (i.e. at the exfoliation nucleation stage). Secondly, in the following exfoliation layer growth stage, there is a lack of systematic and real-time studies on the growing exfoliation layer length versus the important processing parameters, e.g. acoustic pressure, ultrasonic bubbles (including bubble number density), solvent types, processing time, etc.

Here, we present our very recent work on using the ultrafast X-ray phase-contrast imaging (PCI) method (up to 271,554 fps, a temporal resolution of 3.68 μs and a spatial resolution of 1.9 μm/pixel) to study the ultrasonic liquid phase exfoliation dynamics in a bulk graphite material. We used the highly oriented pyrolytic graphite (HOPG), instead of graphite powders or flakes, as the experimental material as argued by Palermo et al. in their work [21]. Because the bulk sheet HOPG samples can be held firmly inside a liquid medium at a fixed location (not moving with the liquid) for X-ray imaging. In addition, the exfoliated layers can be retained at the surface for further ex-situ characterization using, for example, atomic force microscopy (AFM) and electron microscopy.

Approximately 5 Terabit ultrafast X-ray image datasets were acquired through the systematic study, revealing the initiation of the layer exfoliation and the growth dynamics of the exfoliated layers. The real-time experimental observation was complemented by multi-physics numerical simulations to calculate the shock wave produced at bubble implosion and the resulting cyclic and impulsive tensile and shear stresses acting on the graphite surface. The fatigue exfoliation mechanism of graphite layers under the cyclic bombardment of imploding ultrasonic bubbles was revealed and quantified for the first time.

2. Materials and experimental methods

The experiment was carried out at sector 32-ID-B of the Advanced Photon Source (APS) in the hybrid filling operation mode [22,23] (one long electron bunch train of 500 ns plus one short electron bunch of 50 ps as schematically illustrated in Fig. 1a). The white X-ray beam was used in the real-time experiment and it was generated by the short-period (18 mm) undulator with the gaps set at 12.5 mm. The 1st harmonic energy was located at ~24.4 keV with a peak spectral flux of ~6.17×10^{13} phs^{-1}mm^{-2}/0.1% b.w. as shown in Fig. 1b. The sample-to-detector (scintillator) distance was set at ~290 mm. The scintillator was LuAG: Ce, (with 70 ns delay time), and the camera was Photron FastCam SA-Z with a 10× Mitutoyo objective lens. The resulting spatial resolution was 1.9 μm/pixel. In these experiments, three typical imaging frame rates (30,173 fps,135,780 fps and 271,554 fps) were used to image and record the bubble dynamics and bubble interactions with the HOPG sheet. The details of the parameters used are listed in Table 1 below.

The sample arrangement was shown in Fig. 1c. A quartz tube (an outer diameter of 17 mm) was used to hold the liquid media. The HOPG was in a sheet form with a dimension of 10 mm × 10 mm × 2 mm (Agar Scientific, Code AGG3389). It was slotted into the groove of a specially designed quartz sample holder and glued in place by using an HSS12 hot melt adhesive. De-Ionized (DI) water (Fisher Chemical) of 11 ml or a similar amount of NMP (Sigma-Aldrich, Grade≥99.7%) were filled into the quartz tube by using a biocoat disposable syringe. Three K-type thermocouples (250 μm diameter wire, marked as TC1, TC2 and TC3 in Fig. 1c) were used to record the temperatures during the experiment.

TC1 was positioned inside the tube near the top surface of the liquid. TC2 was also inside the tube but inside the cavitation zone. TC3 was positioned at the same height as that of TC2 but on the outside surface of the tube. The quartz tube was then mounted on an X-Y-Z stage (named as the sample stage) at the beamline. A Hielscher UP100H ultrasound generator with a fixed frequency of 30 kHz and a Ti-6Al-4V alloy sonotrode (MS2, 2-mm diameter tip) was used to generate and transmit ultrasonic wave into the liquid. They were mounted on another X-Y-Z stage (named as the ultrasound stage) at the beamline. Through careful manoeuvre and coordination of the two stages, the centre of the sonotrode tip was aligned with the right corner of the HOPG as illustrated in Fig. 2a and b of the Results session. In the experiment, synchronization among the Photron FASTCAM SA-Z camera, the X-ray millisecond mechanical shutter (fast shutter) and the ultrasound generator (UP100H) was made by using three digital delay/pulse generators (Stanford DG535) and setting different time delays on each of them. For a single video recording (i.e. one cycle of the shutter opening and closing) as typically shown in Fig. 2 of the results section, the 'starting' trigger signal (t = 0 s) was passed through a relay box and a transformer to reach the ultrasound generator, the actual sonotrode tip vibration started at approximately t = 298 ms. Before that, the trigger signal reached the camera and X-ray millisecond shutter at approximately t = 255 ms and 294 ms, respectively. Hence, the camera recording started first, then the shutter was opened, and finally, the ultrasound was triggered. After each image sequence recording was completed (i.e. 70 μs recording), the shutter, camera, and ultrasound were closed in reverse order. For continuous recording as shown in Fig. 5, the camera and ultrasound stayed on for a more extended period (at least 1 h), while the slow shutter opened for a specific time interval (i. e. 10 s) for image recording. In this way, the sample and detector were exposed to the X-ray only when the slow shutter was opening. The details of image processing and analysis are in the Supplementary Materials.

3. Results

3.1. Ultrasonic bubble cloud and cavitation zone in DI water and NMP

Fig. 2a and b shows the highly dynamic behaviour of the

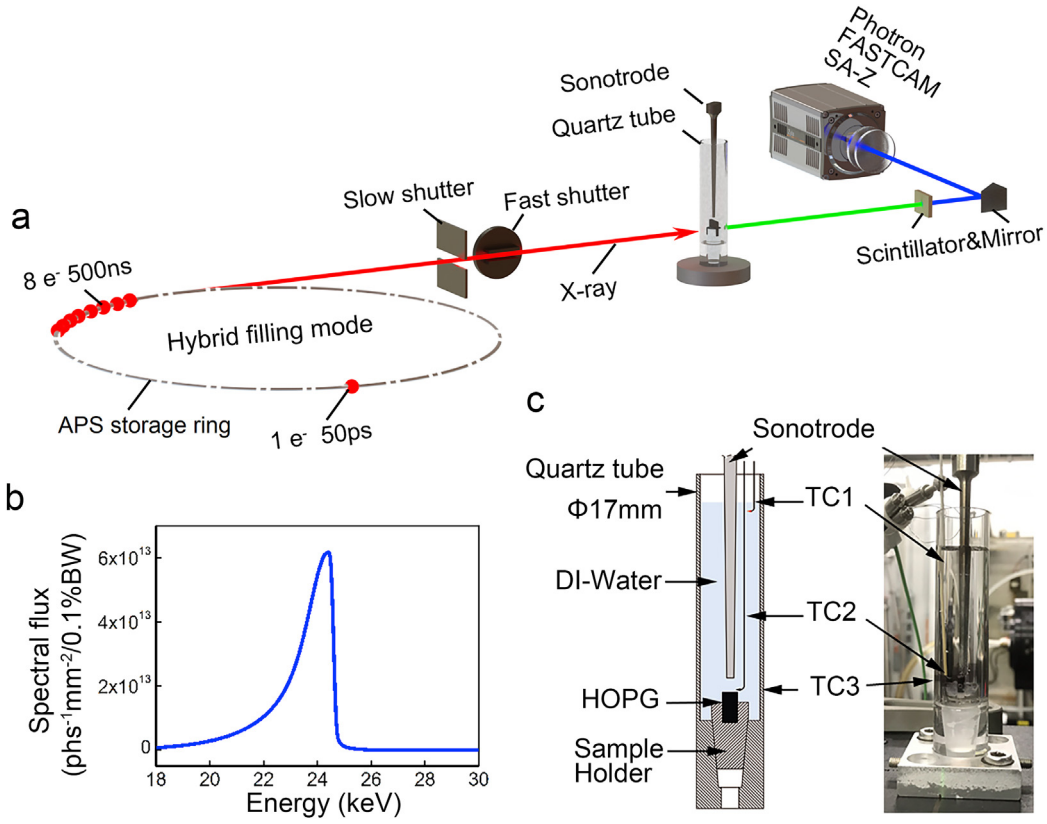

Fig. 1. (a) A schematic of the ultrasonic liquid phase exfoliation experiments conducted in operando conditions at sector 32-ID-B of APS. (b) the spectral photon flux generated by the beamline's short period undulator (U18) set at a 12.5 mm gap. (c) the quartz tube for containing the liquid media (DI water or NMP), the sample holder for holding the HOPG sheets, and the locations of three K-type thermocouples (marked as TC1, TC2 and TC3). (A colour version of this figure can be viewed online.)

Table 1
The X-ray and imaging parameters used in the experiment.

X-ray beam parameters			Imaging parameters (Photron FASTCAM SA-Z)			
Undulator gap (mm)	Peak spectral flux [photons s^{-1} (0.1% bandwidth)$^{-1}$]	Sample-to-detector distance	Acquisition rate (fps)	Image size (pixel × pixel)	Temporal resolution (μs)	Spatial resolution (μm pixel^{-1})
12.5	6.17×10^{13}	290 mm	30,173	768 × 768	33.3	1.9
			135,780	384 × 280	7.4	1.9
			271,554	128 × 70	3.7	1.9

ultrasonic bubbles (a cloud of bubbles) produced by the vibrating sonotrode tip (the black area in Fig. 2a1) in typical four consecutive ultrasonic cycles in DI water and NMP respectively. The bubble clouds formed a highly dynamic bubble cavitation zone as schematically delineated in Fig. 2a2 and 2b2. The bubble cavitation zone observed in NMP (Fig. 2b2) was larger than that in DI water (Fig. 2a2). Video1

Supplementary video related to this article can be found at https://doi.org/10.1016/j.carbon.2021.10.014) (Supplementary Material) illustrates more clearly the highly transient and dynamic movement of the individual bubble and bubble cloud in the cavitation zones, and bubble implosion at the HOPG top surface for the two cases. The bubble behaviour changed rapidly and was cyclically driven by the cyclic ultrasonic pressure field. Bubble implosions occurred in the compressive part of the pressure cycle, producing many hundreds of smaller bubbles (typically seen in Fig. 2a4 and 2b4). A large number of oscillating bubbles inside the bubble clouds were seen to land on the HOPG top surface and imploded, causing the HOPG top layers to expand and contract cyclically in the direction perpendicular to the view field (see Video 1.

for the DI water case in particular). Statistical analysis was also made to calculate the number of bubbles that appeared in the cavitation zone. Fig. 2c shows the area fraction of the bubbles in each X-ray image in Fig. 2a and b, and Fig. 2d shows the corresponding bubble size distribution. In NMP, the average area fraction of the cavitation bubbles was ~54%; while that in DI water was ~37%. The fitted curves in Fig. 2d indicate that the bubble sizes in both cases follow the Lorentz-type distribution. To give a typical example, the total number of bubbles in NMP in Fig. 2b4 was 948, nearly twice that in DI water, 550 (Fig. 2a4). Statistical analysis also indicated that in any ultrasound cycle, on average, approximately 11% (in DI water) and 8.4% (in NMP) of the total number of bubbles in the cavitation zone reached the HOPG surface and imploded.

Supplementary video related to this article can be found at https://doi.org/10.1016/j.carbon.2021.10.014).

In our *in-situ* experiment, the arrangement of the sonotrode tip and HOPG bulk sheet sample is schematically shown in Fig. 3a1. After 10 min of ultrasonic processing, a series of feather-like strips (exfoliated layers) on the surface of HOPG was observed as shown in Fig. 3a2-a6 and Video 2. From the enlarged view of the red

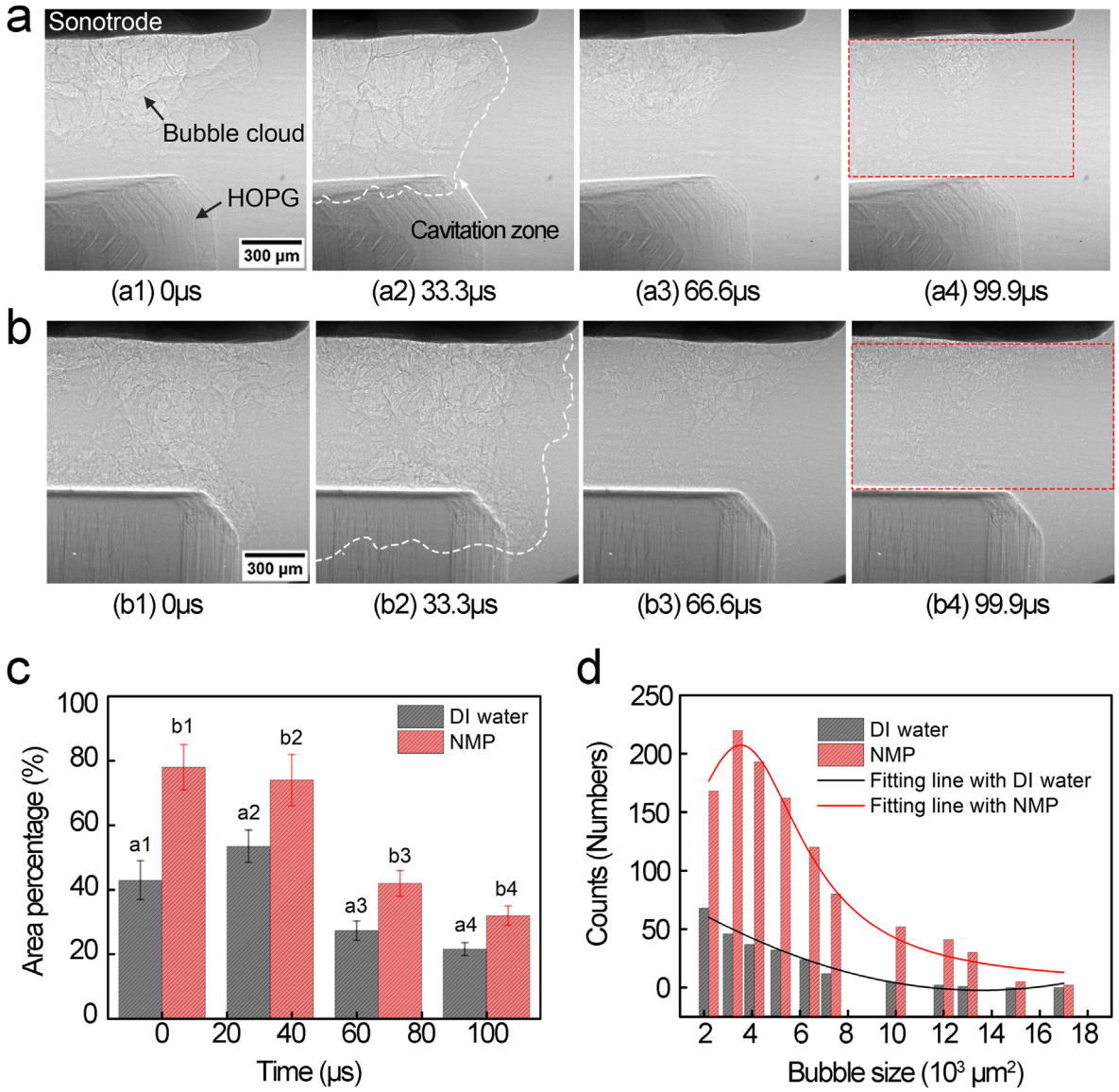

Fig. 2. *Two typical image sequences (captured at 30,173 fps in 4 consecutive ultrasonic cycles), showing the dynamic behaviour of the bubbles cloud in the region between the sonotrode tip and the HOPG top surface in (a) DI water, and in (b) NMP, respectively; (c) The area fraction of the bubbles in the images shown in 2a and 2b, (the baseline area for the calculation is the area directly under the sonotrode tip marked by the red dotted rectangles in Fig. 2a4 and 2b4 respectively); (d) the bubble size distribution calculated from the X-ray images shown in (a4) and (b4), respectively. (All cases are obtained under the measured acoustic power density of 207* W/cm^2*, more dynamic information is illustrated in Video 1).* (A colour version of this figure can be viewed online.)

rectangle in Fig. 3a, cyclic bubble oscillation and implosion were clearly illustrated at the exfoliated boundary (marked by a red arrow). Nearby feather-like strips (exfoliated layers) oscillated according to the oscillation frequency of the bubbles. Video 2 shows such dynamic behaviour more vividly. However, the X-ray image has a spatial resolution of ~2 μm and was not able to resolve the gap between the adjacent exfoliated layers, nor the morphology of the exfoliated layers. Scanning electron microscopy (SEM) examination of the post-processed graphite top and side surfaces (Fig. 3b–e) confirmed that those layers were indeed the split graphite layer bundles with a thickness of 10–20 μm. They were produced by the continuous and cyclic bubble implosion bombardment onto the original lamellar structure (see Fig. 3b). Within different layer bundles, gaps between thin, submicron-sized sheets were also created and expanded, which were most likely the initial sites where graphite layer exfoliation started (see Fig. 3d). There were also many distorted (zig-zag shaped) topological defects appearing at the top surface after 60 min of ultrasound processing (compare Fig. 3b with 3d; as well as Fig. 3c with 3e).

Using the highest frame rate at 271,554 fps (i.e. 3.68 μs between image interval), the dynamic imploding process of an individual bubble at the HOPG top surface in one ultrasonic period was revealed (see Fig. 4a and Video 3

Supplementary video related to this article can be found at https://doi.org/10.1016/j.carbon.2021.10.014, which are extracted from the bubble cloud video sequence). At t = 0 s, the bubble was initially seen on the HOPG top surface with a radius of ~150 μm (Fig. 4a1). It expanded to ~175 μm at 17 μs (Fig. 4a2) in the first expansion half cycle of the pressure wave period. The bubble imploded at 30.6 μs (Fig. 4a5), producing much smaller bubbles or bubble fragments. Subsequently, two bubbles on the HOPG top surface were seen to grow again in the next period (Fig. 4a6).

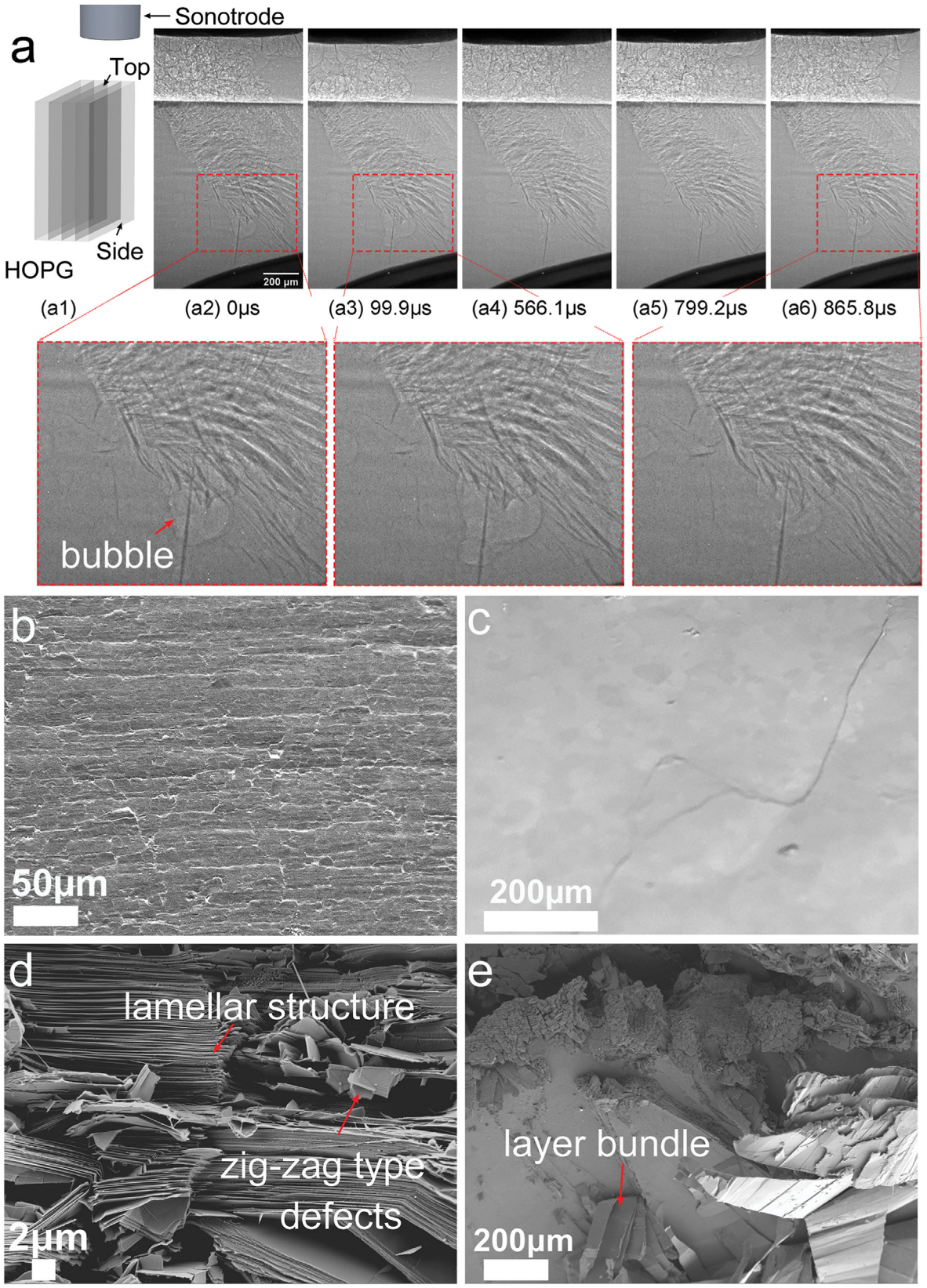

Fig. 3. *(a) A typical image sequence, showing graphite multilayer exfoliation dynamics driven by bubble implosion (at 30,173 fps) and (b)–(e) typical SEM micrographs of the surface characteristics and morphology of the HOPG before and after ultrasound processing in DI water. (b) and (c) show the original conditions of the top surface and the side surface, respectively, before ultrasound processing; (d) shows the de-bonded graphite layers at the top surface after* 60 min *of ultrasound processing; (e) shows the exfoliated graphite layer bundles from the side surface after* 60 min *of ultrasound processing. (More vivid dynamic information can be seen in Video 2).*

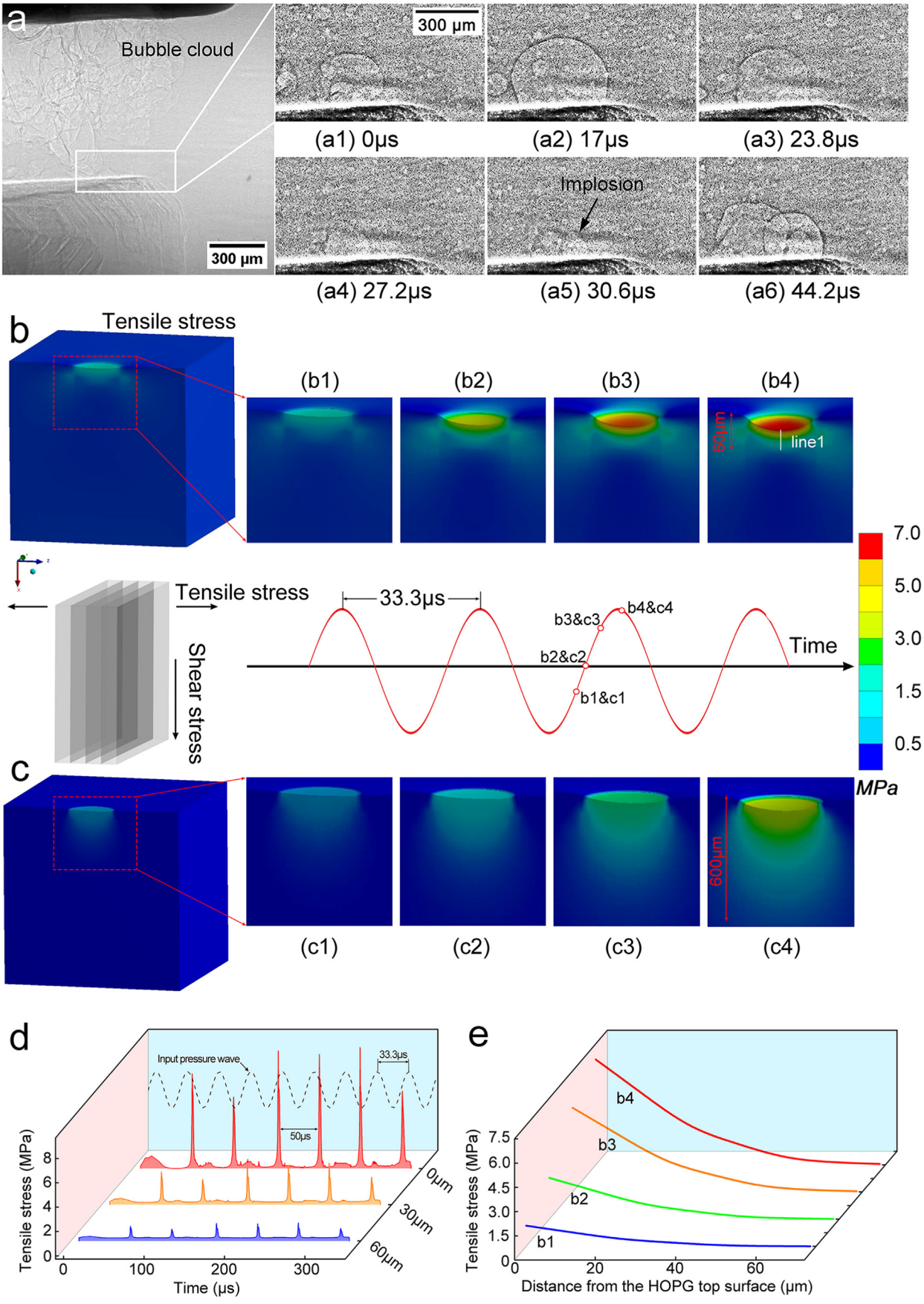
a
Bubble cloud
300 μm
300 μm
(a1) 0μs
(a2) 17μs
(a3) 23.8μs
Implosion
(a4) 27.2μs
(a5) 30.6μs
(a6) 44.2μs
b
Tensile stress
(b1)
(b2)
(b3)
(b4)
60μm
line1
7.0
5.0
3.0
1.5
0.5
MPa
Tensile stress
Shear stress
33.3μs
b3&c3
b4&c4
b2&c2
b1&c1
Time
c
600μm
(c1)
(c2)
(c3)
(c4)
d
Input pressure wave
33.3μs
50μs
0μm
30μm
60μm
Tensile stress (MPa)
Time (μs)
e
b4
b3
b2
b1
Tensile stress (MPa)
Distance from the HOPG top surface (μm)

To fully understand the interaction between imploding bubbles and the graphite surface, we performed a bubble-fluid-structure coupled numerical simulation based on the typically bubble dynamic phenomena as shown in Fig. 4a. The governing equations and numerical methods used are described in detail in the Supplementary Materials. The model is able to calculate the stresses produced at the top surface of the HOPG due to the implosion of an ultrasonic bubble. The stress components parallel and perpendicular to the graphite layers of the HOPG are defined as the shear and tensile stress, respectively. Fig. 4b and c shows that the bubble implosion induced impulsive tensile and shear stresses, respectively, immediately below the HOPG surface. At bubble implosion, the impulsive shear stress propagated ~600 μm deep into the HOPG and reached a peak value of ~3.97 MPa at the HOPG surface. The simulations show that, if a bubble implodes before it touches the top of the HOPG, the calculated shear stress is higher than the tensile stress. When an implosion occurs while the bubble touches the top surface of the HOPG (typically shown in Fig. 4a), the lateral component of the stresses, i.e. the tensile stress is higher than the shear stress. The tensile stress is up to 6.8 MPa and only acts on the surface or at depths of less than 60 μm. Fig. 4e delineates the tensile stress distribution profile from the HOPG top surface to 60 μm below the surface (i.e. along the white line 1 of Fig. 4b4). Its peak values emerged on the surface of HOPG and dramatically decreased with depth. More importantly, under the cyclic ultrasound pressure field, bubble implosions and the resulting impulsive tensile stresses occurred cyclically at the surface as typically indicated in Fig. 4d. The gap between two consecutive stress pulses was calculated as ~50 μs, about ~17 μs longer than one ultrasound period. This extra time was for the pressure wave to propagate through the liquid and then to act onto the HOPG surface. Clearly, such cyclic impulsive stresses imposed a fatigue effect at the HOPG top surface.

3.2. Effects of bubble number density and processing time on multilayer exfoliation

Fig. 5a and b shows two typical X-ray image sequences (at 30,173 fps) acquired during 60 min of ultrasound processing in DI water and NMP, respectively, demonstrating the effects of bubble number density and processing time on multilayer exfoliation dynamics and efficiency. Video 4

Supplementary video related to this article can be found at https://doi.org/10.1016/j.carbon.2021.10.014 (for DI water) and Video 5

Supplementary video related to this article can be found at https://doi.org/10.1016/j.carbon.2021.10.014 (for NMP) show the cyclic movement of the exfoliated multilayers at some typical processing time. In both cases (see Fig. 5a1 for DI water and Fig. 5b1 for NMP, respectively), layer exfoliation started at the top-right edge. A series of feather-like strips appeared and developed as the ultrasonic processing continued. The exfoliated layers became clearer and more visible at the later stage (Fig. 5a4 and 5b4, Video 4 and Video 5). In the X-ray images shown in Fig. 5a and b, there were distinct boundaries (marked by the red arrows) between the original HOPG and the feather-like graphite bundles exfoliated, representing the exfoliated boundary length. The growing length of such boundaries versus time was measured and shown in Fig. 5d. In NMP, the exfoliated boundary length reached 712 μm in the first 10 min, while in DI water, it took ~40 min to reach the peak value (~612 μm). In the region containing the exfoliated feather-like graphite bundles, by drawing a straight line perpendicular to the bundles and analysing the grey value distribution along such line (detailed in the Supplementary Material), we extracted the information about the length and the thickness of each exfoliated graphite layer bundle. Fig. 5e shows the exfoliated length of a single-layer bundle at the three typical points indicated in Fig. 5a3 and 5b3. In NMP it was in the range of 590–940 μm, approximately twice the length of those in DI water (320–410 μm). The difference in the exfoliation rate is presented and discussed in section 4.2. Also, the liquid temperatures were different in the two cases. Fig. 5c shows that the temperature in NMP and DI water reached a relatively constant values of 81 °C and 68 °C after 20min ultrasound processing, respectively.

3.3. Layer exfoliation by the fatigue effect of cyclic impulsive stresses

To understand quantitatively the fatigue effect on HOPG layer exfoliation due to the impulsive stresses, we established the fatigue tensile stress – fatigue life relationship (the S –N curve) for the HOPG layer using the equations below:

$$N = CS^{-\psi} \tag{1}$$

$$\lg N = \lg C - \psi \lg S \tag{2}$$

Where S is the fatigue tensile stress, N is the number of cycles to failure, C and ψ are the material constants. We used the very rich fatigue datasets obtained from the pile grade X (PGX) graphite to establish the $S - N$ relationship [24]. Fig. 6a shows the referenced data (black crosses) and the fitted $S - N$ curve, expressed in the number of ultrasound cycles as well as the actual ultrasonic processing time. $\psi$and$C$were calculated as 47.07 and 1.66 × 10^{44} respectively. In addition, the averaged exfoliated layer lengths for the two cases as a function of ultrasound processing time are shown in Fig. 6b. The actual cavitation bubble zones are also drawn schematically in Fig. 6b for easy comparison.

Fig. 6a clearly illustrates that, at a given tensile stress level, for the graphite directly below an imploding bubble, layer exfoliation (i. e. debonding or breaking of graphite layers) occurs when the ultrasonic processing time (or a number of ultrasound cycles) exceeds its fatigue life. As described in Fig. 6a and Fig. S2 (Supplementary Materials), the magnitude and frequency of the impulsive stresses are closely linked to the conditions of the imploding bubbles, i.e. the size and number density of the bubbles and the pressure field in the cavitation zone. Brown S–N curve represents the fatigue exfoliation behaviour of the HOPG under the continuous implosion impact of a single bubble. On this curve, the red dotted-line box indicates that at a stress level of 6.8–7.1 MPa, layer exfoliation occurs in 1–10 s. While at the tensile stress level of 6.2–6.5 MPa (the green dotted-line box), exfoliation occurs in 1–10 min. Statistical analysis of the bubble behaviour shows that, in an ultrasound cycle, approximately 11% (60 bubbles in DI water) and 8.4% (80 bubbles in NMP) of the total number of bubbles in the cavitation zone landed on the surface of HOPG and imploded. Statistically, the probability of the bubble landed and imploded at any particular location on the HOPG surface are equal. Hence, in any one ultrasound cycle in the studied conditions, there were ~16

Fig. 4. (a) A sequence of X-ray images in one ultrasonic period in DI water (at 271,554 fps), showing the oscillation and implosion of a single bubble at the HOPG top surface. A bubble-fluid-structure coupled numerical modelling was developed (See the Supplementary Materials for details), and the time evolved tensile stress (b1)-(b4) and shear stress (c1)-(c4) distributions in HOPG materials induced by the single bubble implosion. (d) Shows the impulsive tensile stress profiles in 10 ultrasound cycles due to bubble implosion (data were extracted at 0 μm, 30 μm and 60 μm below the HOPG top surface as indicated by line 1 in Fig. 4b4). (e) In a single ultrasound cycle, the time-evolved tensile stress profiles along line 1 in Fig. 4b1-4b4. (A colour version of this figure can be viewed online.)

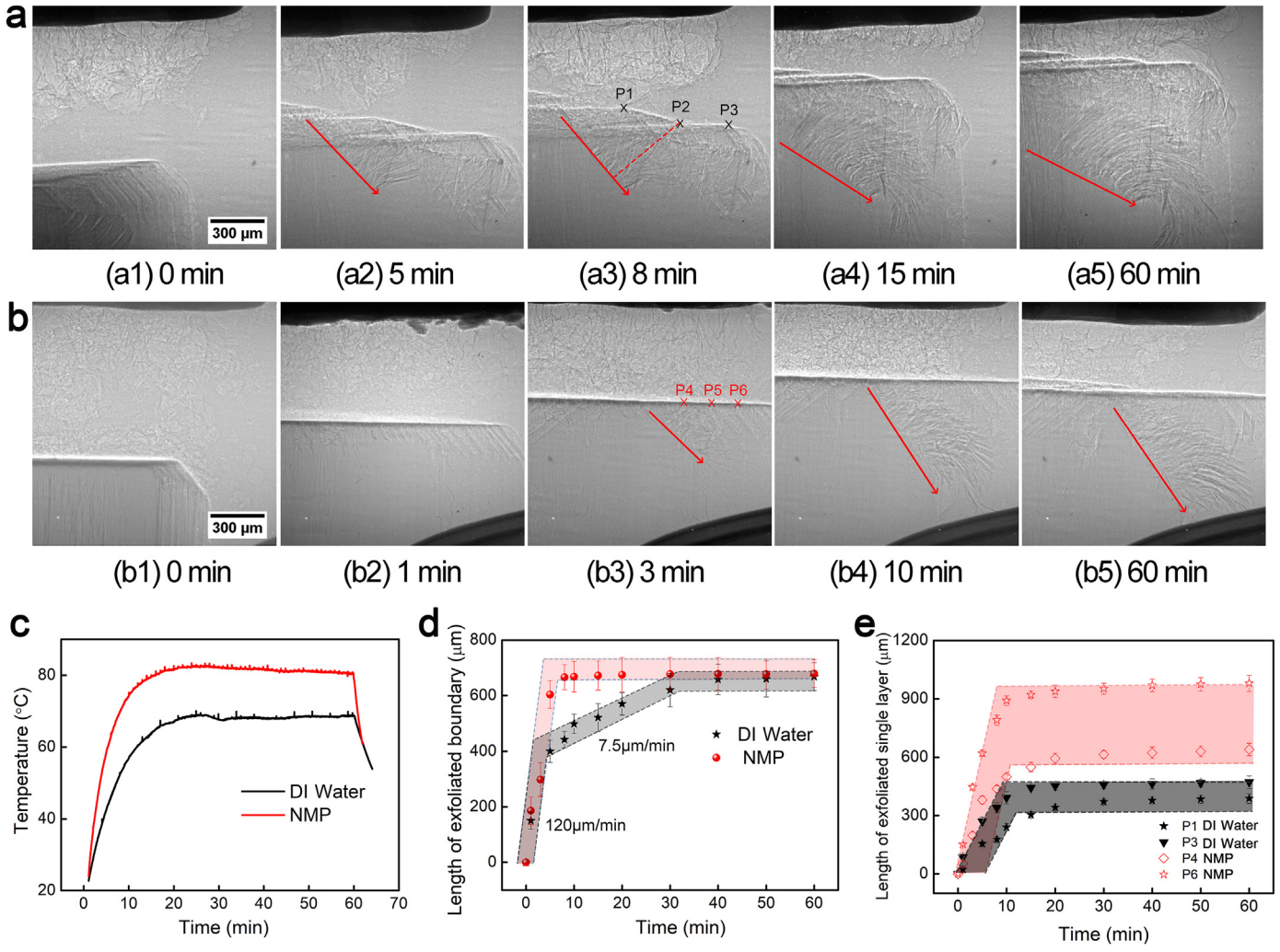

Fig. 5. Two typical image sequences (at 30,173 fps), showing the HOPG multilayer exfoliation process in 60 min of ultrasound processing in (a) DI water, and (b) NMP respectively and the red arrows show the boundary of an exfoliated area. (c) the liquid temperature profiles recorded by the thermocouple, TC2; (d) the length of the exfoliated boundary (length of red arrows in (a) and (b)). (e) The length of the exfoliated individual layer bundle (for example, the length of the dotted line connecting point P2 and the exfoliated boundary was considered as the exfoliated layer length at P2, similarly for points, P1, P3, etc.) as a function of processing time. (More dynamic information can be seen in Videos 4 and 5). (A colour version of this figure can be viewed online.)

bubbles imploding at the same location for the case of DI water, and ~22 bubbles for the case of NMP. The fatigue exfoliation behaviour due to such multiple bubbles implosion effect is reflected by the light green and light purple S–N curves in Fig. 6a. For example, at a fatigue stress of 6.2 MPa (indicated by the dotted red line in Fig. 6a), the time needed for layer exfoliation to occur due to the fatigue effect of a single bubble was 10 min. In the actual condition with the fatigue effect from multiple bubbles implosion, the time for exfoliation was shortened to 0.83 min in DI water and 0.62 min in NMP. Furthermore, Fig. 6b (the data were reproduced from those shown in Fig. 5e) clearly illustrates that the layer exfoliation length increased almost linearly with the processing time inside the cavitation zone. It reached the maximum lengths for both cases approximately in the first 10 min of ultrasonic processing. Outside the cavitation zone, layer exfoliation events effectively stopped.

4. Discussion

4.1. Fatigue mechanisms of ultrasonic exfoliation in liquid

The liquid exfoliation mechanisms of bulk 2D materials under ultrasound have been a subject of intensive research and debate for more than a decade. Previously, the generally accepted hypothesis is that the alternating acoustic pressure field causes sudden collapse of cavitation bubbles, producing micro jets and shock waves which could impose compressive stress onto the bulk 2D layers. The compressive stress could turn into tensile stress after propagation from one surface to the opposite surface, pulling apart the 2D layers and overcoming the energy barrier to achieve exfoliation. For individual flakes, the microjets and shock waves were also identified as the driving force for further fragmentation [14,25]. Very recently, Li et al. [16] and Backes et al. [26] also revealed that 5 s of acoustic-pressure exposure could rupture large graphite flakes and form kink band striations on the flake surfaces. Then cracks could initiate along these striations, and together with intercalation of solvent, lead to the unzipping and peeling off of thin graphite strips. However, those hypotheses and explanations were mostly based on post-processing microstructural analyses, lacking the real-time obtained *in situ* evidence. Our real-time investigation showed that the applied ultrasonic pressure wave and bubble implosion played different roles in the process of layer exfoliation and was far more complicated than previously

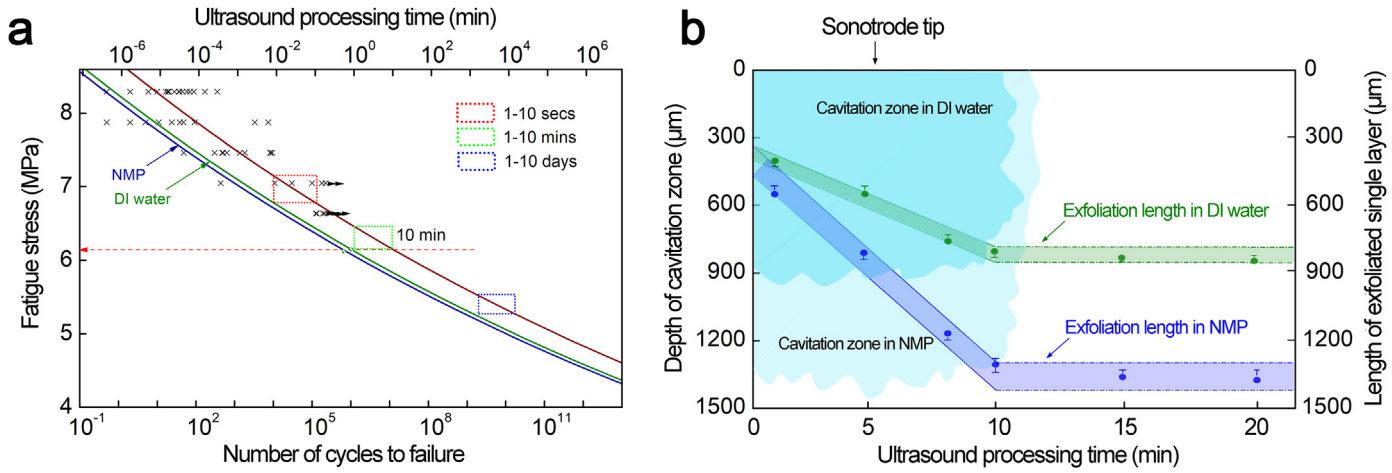

Fig. 6. (a) The S–N curve (the brown curve) obtained by fitting the graphite fatigue data (black crosses) referenced from [24]. It represents the S–N curve of the HOPG due to the fatigue effect of a single imploding bubble. The other two S–N curves consider the actual number of imploding bubbles at the HOPG surface in DI water (the light green curve) and NMP (the light purple curve) respectively. (b) The average length of the exfoliated layers as a function of ultrasound processing time in DI water and NMP, respectively. The data were averaged from the measured exfoliation length data illustrated in Fig. 5e. The cavitation bubble zones (the colour-shaded areas) are also shown in (b), indicating clearly that layer exfoliation events occur inside the cavitation zone. (A colour version of this figure can be viewed online.)

suggested. In the studied condition, the acoustic pressure transmitted through the liquid onto the HOPG top surface was normally lower than ~1 MPa (see Fig. S2 in Supplementary Materials). It would be impossible for such low pressure to cause any mechanical breakdown of the HOPG sheets (see Fig. 6a). The bubble implosion, on the other hand, played the dominant role in exfoliation. The continuous bubble bombardment and implosions at the HOPG top surface produced repetitive and impulsive stresses in par with the ultrasound period. The tensile stress induced by bubble implosion mostly acts on the surface or at depths less than 300 μm, such tensile stresses were in the range of 3–7 MPa, adequate to expand the interlayers spacing and produce breakdown for the layers at the top surface in the early stage of exfoliation. This simulated stress range is very close to the theoretical estimate in the previous study [15,27]. The tensile stresses continue to act on the junctions between the exfoliated layer and the original bulk material when exfoliation starts. The unique advantage of ultrasonic processing is that if the points of exfoliation remained inside the cavitation zone, such points would be subject to continuous multiple bubble implosion. The exfoliation rate is multiplied by the number of bubbles imploded at the same location. Hence the exfoliation rate could be accelerated tens of or even hundreds of times by controlling the number density of the bubbles in the cavitation zone, which can be easily achieved by optimizing the ultrasound parameters for maximizing cavitation bubbles. For example, in the case of the DI water, the number of bubbles in a single wave period was about 550, and statistically, 11% of these bubbles reached the HOPG surface and then imploded. This means that there were 16 implosion events at one particular location in each wave period that accelerated the fatigue exfoliation by a factor of 16 times as indicated by the light green S–N curve in Fig. 6a. Similarly, a light purple S–N curve in Fig. 6a shows the NMP case. Such new insight can only be revealed by real-time and *in situ* studies. Any previous post-processing structural analyses cannot provide such dynamic information. Fig. 6b also clearly indicates that within the cavitation zone where continuous and sufficient supply of imploding bubbles was maintained, the exfoliation rate was sustained at a constant rate for both cases, until the location for exfoliation moved out of the cavitation zone. The X-ray images and videos showed that the cavitation bubble zone was larger in NMP than that in DI water and the bubble number density in NMP was nearly double that in DI water, resulting in 2.26 times more bubbles imploding at the surface of HOPG. Hence, the average exfoliation rate in NMP (76.5 μm/min) was almost twice that in DI water (36.5 μm/min). Clearly, the number density of bubbles is the dominant factor for the layer fatigue exfoliation. The fatigue mechanisms discussed above are applicable to the bulk HOPG and other graphite sheet materials as well. For other forms of graphite materials, e.g. powers or flakes, further real-time investigations are underway and the new findings will be reported elsewhere separately.

4.2. *Effects of solvent and ultrasound processing time on layer exfoliation*

A number of studies have been conducted to investigate the role of solvents in ultrasonic exfoliation [28–31]. It was suggested that the solvents generated an energy barrier to prevent neighbouring graphene sheets from aggregation while the exfoliation dynamics was not affected [32]. In our study, Fig. 5e demonstrated that the exfoliation rate in NMP was higher than in DI water. The faster exfoliation rate in NMP is caused by the higher density of cavitation bubbles in NMP than in that in DI water as discussed in the previous section. The higher number of bubbles generated in NMP is due to the low vaporization pressure threshold in NMP, which is a critical parameter for the generation of cavitation bubbles. The vaporization pressure threshold of NMP is 0.3466 mmHg at 25 °C, 68.3 times lower than that of DI water (23.68 mm Hg at 25 °C) [33]. Hence, the energy required to form cavitation bubbles in NMP is significantly lower than that needed in DI water. As the results, under the same ultrasound input power condition, much more bubbles were produced in the NMP than those in the DI water. In addition, the depth of the cavitation zone in NMP was 1440 μm and that in DI water was 921 μm. This also explains why the length of the exfoliated single layer was longer in NMP than that in DI water as shown in Figs. 5e and 6b.

5. Conclusions

The dynamic mechanisms of ultrasound liquid exfoliation of bulk graphite sheet material have been studied in operando conditions by ultrafast synchrotron X-ray imaging, complemented by multiphysics numerical modelling. The key findings of the research

are:

1. The exfoliation dynamics under periodic bombardment of ultrasonic bubble implosion were observed and revealed *in situ* for the first time using a special in-operando experimental appratus and ultrafast X-ray imaging. Bubble implosion created cyclic impulsive tensile and shear stresses into the graphite with a peak value up to 6.8 MPa, producing very efficient graphite layer exfoliation occurring in a fatigue manner in a time scale from seconds to minutes.
2. The layer exfoliation rate and efficiency were predominantly determined by the number of imploding bubbles inside the effective cavitation bubble zone. In the studied conditions, the number density of the ultrasonic bubbles in NMP was nearly doubled than that in DI water, resulted in an average graphite layer exfoliation rate of 76.5 μm/min in NMP as compared to 36.5 μm/min in DI water.

CRediT authorship contribution statement

Ling Qin: Conceptualization, Data curation, Methodology, Software, Investigation, Validation, Visualization, Writing – original draft. **Barbara M. Maciejewska:** Investigation, Writing – review & editing. **Tungky Subroto:** Investigation, Writing – review & editing. **Justin A. Morton:** Investigation, Writing – review & editing. **Kyriakos Porfyrakis:** Funding acquisition, Writing – review & editing. **Iakovos Tzanakis:** Funding acquisition, Writing – review & editing. **Dmitry G. Eskin:** Funding acquisition, Writing – review & editing. **Nicole Grobert:** Resources, Funding acquisition, Writing – review & editing. **Kamel Fezzaa:** Investigation, Writing – review & editing. **Jiawei Mi:** Conceptualization, Methodology, Funding acquisition, Project administration, Resources, Supervision, Writing – review & editing.

Declaration of competing interest

The authors declare that they have no known competing financial interests or personal relationships that could have appeared to influence the work reported in this paper.

Acknowledgements

The authors would like to acknowledge the financial support from the UK Engineering and Physical Sciences Research Council (Grant Nos. EP/R031665/1; EP/R031401/1; EP/R031819/1; EP/R031975/1). This research used resources of the Advanced Photon Source, a U.S. Department of Energy (DOE) Office of Science User Facility operated for the DOE Office of Science by Argonne National Laboratory under Contract No.DE-AC02-06CH11357. We also would like to acknowledge the uses of the Viper High-Performance Computing (HPC) Facility of the University of Hull and its technical team (Mr Chris Collins in particular) for the support on computing and simulation related work. Nicole Grobert would like to thank the Royal Society for its financial support.

Appendix A. Supplementary data

Supplementary data to this article can be found online at https://doi.org/10.1016/j.carbon.2021.10.014.

References

[1] D. Akinwande, C. Huyghebaert, C.-H. Wang, M.I. Serna, S. Goossens, L.-J. Li, H.-S.P. Wong, F.H. Koppens, Graphene and two-dimensional materials for silicon technology, Nature 573 (7775) (2019) 507–518, https://doi.org/10.1038/s41586-019-1573-9.
[2] D. Deng, K. Novoselov, Q. Fu, N. Zheng, Z. Tian, X. Bao, Catalysis with two-dimensional materials and their heterostructures, Nat. Nanotechnol. 11 (3) (2016) 218–230, https://doi.org/10.1038/nnano.2015.340.
[3] D.V. Andreeva, M. Trushin, A. Nikitina, M.C. Costa, P.V. Cherepanov, M. Holwill, S. Chen, K. Yang, S.W. Chee, U. Mirsaidov, Two-dimensional adaptive membranes with programmable water and ionic channels, Nat. Nanotechnol. 16 (2) (2021) 174–180, https://doi.org/10.1038/s41565-020-00795-y.
[4] C.-X. Hu, Y. Shin, O. Read, C. Casiraghi, Dispersant-assisted liquid-phase exfoliation of 2D materials beyond graphene, Nanoscale 13 (2) (2021) 460–484, https://doi.org/10.1039/D0NR05514J.
[5] A. Amiri, M. Naraghi, G. Ahmadi, M. Soleymaniha, M. Shanbedi, A review on liquid-phase exfoliation for scalable production of pure graphene, wrinkled, crumpled and functionalized graphene and challenges, FlatChem 8 (2018) 40–71, https://doi.org/10.1016/j.flatc.2018.03.004.
[6] A.V. Tyurnina, I. Tzanakis, J. Morton, J. Mi, K. Porfyrakis, B.M. Maciejewska, N. Grobert, D.G. Eskin, Ultrasonic exfoliation of graphene in water: a key parameter study, Carbon 168 (2020) 737–747, https://doi.org/10.1016/j.carbon.2020.06.029.
[7] Z. Xie, C. Xing, W. Huang, T. Fan, Z. Li, J. Zhao, Y. Xiang, Z. Guo, J. Li, Z. Yang, Ultrathin 2D nonlayered tellurium nanosheets: facile liquid-phase exfoliation, characterization, and photoresponse with high performance and enhanced stability, Adv. Funct. Mater. 28 (16) (2018), 1705833, https://doi.org/10.1002/adfm.201705833.
[8] D. Parviz, F. Irin, S.A. Shah, S. Das, C.B. Sweeney, M.J. Green, Challenges in liquid-phase exfoliation, processing, and assembly of pristine graphene, Adv. Mater. 28 (40) (2016) 8796–8818, https://doi.org/10.1002/adma.201601889.
[9] P. He, C. Zhou, S. Tian, J. Sun, S. Yang, G. Ding, X. Xie, M. Jiang, Urea-assisted aqueous exfoliation of graphite for obtaining high-quality graphene, Chem. Commun. 51 (22) (2015) 4651–4654, https://doi.org/10.1039/C5CC00059A.
[10] S. Haar, M. El Gemayel, Y. Shin, G. Melinte, M.A. Squillaci, O. Ersen, C. Casiraghi, A. Ciesielski, P. Samorì, Enhancing the liquid-phase exfoliation of graphene in organic solvents upon addition of n-octylbenzene, Sci. Rep. 5 (1) (2015) 1–9, https://doi.org/10.1038/srep16684.
[11] J.T. Han, J.I. Jang, H. Kim, J.Y. Hwang, H.K. Yoo, J.S. Woo, S. Choi, H.Y. Kim, H.J. Jeong, S.Y. Jeong, Extremely efficient liquid exfoliation and dispersion of layered materials by unusual acoustic cavitation, Sci. Rep. 4 (1) (2014) 1–7, https://doi.org/10.1038/srep05133.
[12] J.-H. Ding, H.-R. Zhao, H.-B. Yu, A water-based green approach to large-scale production of aqueous compatible graphene nanoplatelets, Sci. Rep. 8 (1) (2018) 1–8, https://doi.org/10.1038/s41598-018-23859-5.
[13] X. Cui, C. Zhang, R. Hao, Y. Hou, Liquid-phase exfoliation, functionalization and applications of graphene, Nanoscale 3 (5) (2011) 2118–2126, https://doi.org/10.1039/C1NR10127G.
[14] P. Turner, M. Hodnett, R. Dorey, J.D. Carey, Controlled sonication as a route to in-situ graphene flake size control, Sci. Rep. 9 (1) (2019) 1–8, https://doi.org/10.1038/s41598-019-45059-5.
[15] A. Alaferdov, A. Gholamipour-Shirazi, M. Canesqui, Y.A. Danilov, S. Moshkalev, Size-controlled synthesis of graphite nanoflakes and multi-layer graphene by liquid phase exfoliation of natural graphite, Carbon 69 (2014) 525–535, https://doi.org/10.1016/j.carbon.2013.12.062.
[16] Z. Li, R.J. Young, C. Backes, W. Zhao, X. Zhang, A.A. Zhukov, E. Tillotson, A.P. Conlan, F. Ding, S.J. Haigh, Mechanisms of liquid-phase exfoliation for the production of graphene, ACS Nano 14 (9) (2020) 10976–10985, https://doi.org/10.1021/acsnano.0c03916.
[17] X. Ma, B. Huang, Y. Li, Q. Chang, S. Qiu, Z. Su, X. Fu, G. Wang, Numerical simulation of single bubble dynamics under acoustic travelling waves, Ultrason. Sonochem. 42 (2018) 619–630, https://doi.org/10.1016/j.ultsonch.2017.12.021.
[18] G. Servant, J.P. Caltagirone, A. Gérard, J.L. Laborde, A. Hita, Numerical simulation of cavitation bubble dynamics induced by ultrasound waves in a high frequency reactor, Ultrason. Sonochem. 7 (4) (2000) 217–227, https://doi.org/10.1016/S1350-4177(00)00059-6.
[19] V. Sresht, A.A. Padua, D. Blankschtein, Liquid-phase exfoliation of phosphorene: design rules from molecular dynamics simulations, ACS Nano 9 (8) (2015) 8255–8268, https://doi.org/10.1021/acsnano.5b02683.
[20] C.-J. Shih, S. Lin, M.S. Strano, D. Blankschtein, Understanding the stabilization of liquid-phase-exfoliated graphene in polar solvents: molecular dynamics simulations and kinetic theory of colloid aggregation, J. Am. Chem. Soc. 132 (41) (2010) 14638–14648, https://doi.org/10.1021/ja1064284.
[21] Z.Y. Xia, S. Pezzini, E. Treossi, G. Giambastiani, F. Corticelli, V. Morandi, A. Zanelli, V. Bellani, V. Palermo, The exfoliation of graphene in liquids by electrochemical, chemical, and sonication-assisted techniques: a nanoscale study, Adv. Funct. Mater. 23 (37) (2013) 4684–4693, https://doi.org/10.1002/adfm.201203686.
[22] Y. Wang, X. Liu, K.-S. Im, W.-K. Lee, J. Wang, K. Fezzaa, D.L.S. Hung, J.R. Winkelman, Ultrafast X-ray study of dense-liquid-jet flow dynamics using structure-tracking velocimetry, Nat. Phys. 4 (4) (2008) 305–309, https://doi.org/10.1038/nphys840.
[23] B. Wang, D.Y. Tan, T.L. Lee, J.C. Khong, F. Wang, D. Eskin, T. Connolley, K. Fezzaa, J. Mi, Ultrafast synchrotron X-ray imaging studies of microstructurefragmentation in solidification under ultrasound, Acta Mater. 144 (2018) 505–515, https://doi.org/10.1016/j.actamat.2017.10.067.
[24] M. Eto, T. Arai, T. Konishi, The Fatigue Strength of Graphite and Carbon

Materials for HTTR Core Components, Japan Atomic Energy Research Inst., 1998.
[25] H. Ma, Z. Shen, S. Ben, Understanding the exfoliation and dispersion of MoS2 nanosheets in pure water, J. Colloid Interface Sci. 517 (2018) 204–212, https://doi.org/10.1016/j.jcis.2017.11.013.
[26] C. Backes, D. Campi, B.M. Szydlowska, K. Synnatschke, E. Ojala, F. Rashvand, A. Harvey, A. Griffin, Z. Sofer, N. Marzari, Equipartition of energy defines the size–thickness relationship in liquid-exfoliated nanosheets, ACS Nano 13 (6) (2019) 7050–7061, https://doi.org/10.1021/acsnano.9b02234.
[27] B.Z. Jang, A. Zhamu, Processing of nanographene platelets (NGPs) and NGP nanocomposites: a review, J. Mater. Sci. 43 (15) (2008) 5092–5101, https://doi.org/10.1007/s10853-008-2755-2.
[28] X. Hai, K. Chang, H. Pang, M. Li, P. Li, H. Liu, L. Shi, J. Ye, Engineering the edges of MoS2 (WS2) crystals for direct exfoliation into monolayers in polar micromolecular solvents, J. Am. Chem. Soc. 138 (45) (2016) 14962–14969, https://doi.org/10.1021/jacs.6b08096.
[29] G.-Q. Han, Y.-R. Liu, W.-H. Hu, B. Dong, X. Li, Y.-M. Chai, Y.-Q. Liu, C.-G. Liu, WS2 nanosheets based on liquid exfoliation as effective electrocatalysts for hydrogen evolution reaction, Mater. Chem. Phys. 167 (2015) 271–277, https://doi.org/10.1016/j.matchemphys.2015.10.043.
[30] M. Lotya, Y. Hernandez, P.J. King, R.J. Smith, V. Nicolosi, L.S. Karlsson, F.M. Blighe, S. De, Z. Wang, I.T. McGovern, G.S. Duesberg, J.N. Coleman, Liquid phase production of graphene by exfoliation of graphite in surfactant/water solutions, J. Am. Chem. Soc. 131 (10) (2009) 3611–3620, https://doi.org/10.1021/ja807449u.
[31] K.-G. Zhou, N.-N. Mao, H.-X. Wang, Y. Peng, H.-L. Zhang, A mixed-solvent strategy for efficient exfoliation of inorganic graphene analogues, Angew. Chem. Int. Ed. 50 (46) (2011) 10839–10842, https://doi.org/10.1002/ange.201105364.
[32] C. Fu, X. Yang, Molecular simulation of interfacial mechanics for solvent exfoliation of graphene from graphite, Carbon 55 (2013) 350–360, https://doi.org/10.1016/j.carbon.2012.12.083.
[33] J.-P. Franc, J.-M. Michel, Fundamentals of Cavitation, vol. 76, Springer science & Business media, 2006.